Microsc. Microanal. 21, 946–952, 2015
doi:10.1017/S1431927615013732

Microscopy AND Microanalysis

© MICROSCOPY SOCIETY OF AMERICA 2015

Accurate Nanoscale Crystallography in Real-Space Using Scanning Transmission Electron Microscopy

J. Houston Dycus,[1] Joshua S. Harris,[1] Xiahan Sang,[1] Chris M. Fancher,[1] Scott D. Findlay,[2] Adedapo A. Oni,[1] Tsung-ta E. Chan,[1] Carl C. Koch,[1] Jacob L. Jones,[1] Leslie J. Allen,[3] Douglas L. Irving,[1] and James M. LeBeau[1,*]

[1]*Department of Materials Science and Engineering, North Carolina State University, Raleigh, NC 27695, USA*
[2]*School of Physics and Astronomy, Monash University, Clayton, VIC 3800, Australia*
[3]*School of Physics, University of Melbourne, Parkville, VIC 3010, Australia*

Abstract: Here, we report reproducible and accurate measurement of crystallographic parameters using scanning transmission electron microscopy. This is made possible by removing drift and residual scan distortion. We demonstrate real-space lattice parameter measurements with <0.1% error for complex-layered chalcogenides Bi_2Te_3, Bi_2Se_3, and a $Bi_2Te_{2.7}Se_{0.3}$ nanostructured alloy. Pairing the technique with atomic resolution spectroscopy, we connect local structure with chemistry and bonding. Combining these results with density functional theory, we show that the incorporation of Se into Bi_2Te_3 causes charge redistribution that anomalously increases the van der Waals gap between building blocks of the layered structure. The results show that atomic resolution imaging with electrons can accurately and robustly quantify crystallography at the nanoscale.

Key words: scanning transmission electron microscopy, atomic resolution spectroscopy, nanoscale metrology, Bi_2Te_3

Introduction

Over the past century powder diffraction has proven an invaluable tool for investigating the structure of materials (Thomas, 2012). Because the material's three-dimensional information is compressed into a one-dimensional signal, as shown in Figure 1a, direct access to important nanoscale details such as grain boundary structure, chemical segregation, and local distortion is lost (Billinge & Levin, 2007; Page et al., 2010; Esteves et al., 2014). As a prototypical example, consider the Bi_2Te_3-based thermoelectric nanocomposites where the crystal structure is comprised of Group V (Bi) and VI (Te) elements with three quintuple VI^1-Bi-VI^2-Bi-VI^1 layers in a unit cell. VI^2-Bi and Bi-VI^1 are strong iono-covalent bonds, while the VI^1-VI^1 bond is dominated by weak van der Waals forces. Recent success with nanostructuring Bi_2Te_3-based alloys has led to dramatically enhanced thermoelectric behavior resulting from a combination of nanoscale mechanisms (Poudel et al., 2008; Lan et al., 2009; Martin et al., 2009). Therefore, the quantitative investigation of their atomic structure is required to completely understand the behavior of these materials.

In contrast to synchrotron diffraction, aberration-corrected electron microscopes are capable of imaging both structure and chemistry directly at the atomic scale. Furthermore, the spatial resolution of transmission electron microscopy (TEM) spans from the micrometer to ångström length scales, as highlighted in Figures 1b and 1c, and enables real-space structure quantification. High-angle annular dark-field scanning transmission electron microscopy (HAADF STEM) is a particularly powerful technique for resolving the atomic structure, with image intensities that correspond to both the type and total number of atoms present (Pennycook & Nellist, 2011; Dycus et al., 2013). For quantitative distance measurements, however, the raster imaging process significantly reduces measurement accuracy due to scan artifacts, thermal drift, and residual scan system distortion. Although recent advances in STEM imaging methods have enabled picometer-level *precision*, *accurate* distance measurements have required an area of known structure to be available in the same image (Kimoto et al., 2010; Kim et al., 2012; Sang & LeBeau, 2014; Yankovich et al., 2014). One method in particular, revolving STEM (RevSTEM), encodes all the information necessary to accurately quantify and subsequently remove drift-induced distortion present in each frame (Sang & LeBeau, 2014). Beyond sample drift-induced distortion, however, residual distortion is also introduced from slight deviations of scan coil strengths. This scan system distortion introduces skewing, expansion, and/or contraction globally across the image and further limits measurement accuracy.

In this article, we apply RevSTEM to quantify the crystallography of layered, large unit-cell compounds with the Bi_2Te_3 crystal structure (Sang & LeBeau, 2014). To do so, we introduce a calibration scheme that corrects for residual scan distortion in RevSTEM images. We demonstrate that crystallographic measurements with better than 0.1% accuracy for Bi_2Te_3, Bi_2Se_3, and a nanostructured $Bi_2Te_{2.7}Se_{0.3}$ alloy can be achieved without the need for an internal sample reference. We compare our RevSTEM results to X-ray diffraction (XRD) measurements using the same source

Received January 20, 2015; accepted May 29, 2015
**Corresponding author.* jmlebeau@ncsu.edu

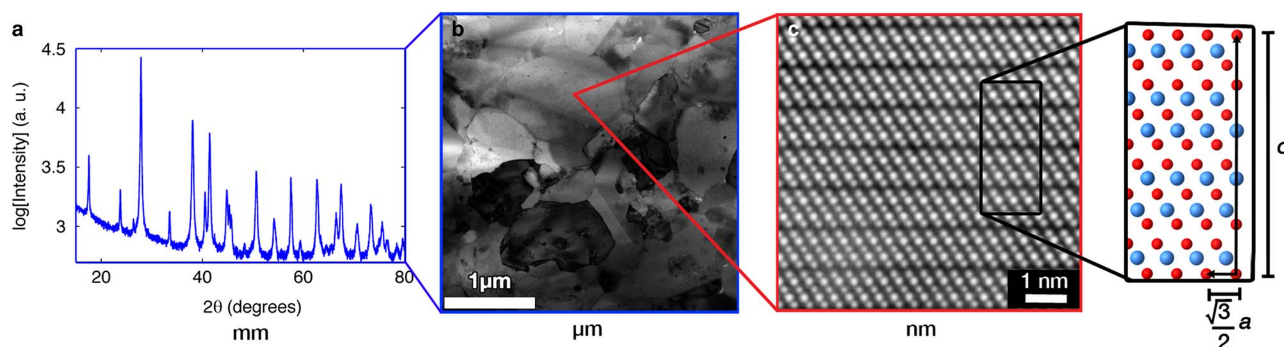

Figure 1. (**a**) Powder diffraction pattern of a typical $Bi_2Te_{2.7}Se_{0.3}$ nanocomposite sample with corresponding (**b**) bright-field TEM and (**c**) high-angle annular dark-field STEM images (probe convergence semi-angle 13.5 mrad). A schematic of the projected unit cell [bismuth (blue)/tellurium (red)] is also provided.

material and to prior literature. Extending this analysis, we determine local alloy composition to within 1 at% using Vegard's law and directly quantify atom positions within the unit cell (Denton & Ashcroft, 1991). Further, we report an anomalous increase in the van der Waals gap of the alloy sample and use density functional theory (DFT) to show that charge redistribution is the mechanism responsible for this behavior.

Materials and Methods

STEM

Samples of Bi_2Te_3 and Bi_2Se_3 with 99.999% purity were acquired from MTI Corporation (Richmond, CA) and Sigma Aldrich (St. Louis, MO), respectively. Small flakes were cleaved from the sample bulk. Cross-sectional samples were produced by adhering the flakes to square pieces of Si <100> wafer using M-bond 610 adhesive. Nanostructured thermoelectric alloy powders were fabricated by high-energy ball milling and mechanical alloying elemental powders with nominal composition $Bi_2Te_{2.7}Se_{0.3}$ by the process outlined in Chan et al. (2013). Each sample was mechanically polished to electron transparency with an Allied Multiprep^{TM} system and cleaned with a Fishione Model 1050 argon ion mill at LN_2 temperature. A probe corrected FEI (Hillsboro, OR) G2 60–300 kV S/TEM equipped with a high brightness X-FEG electron source was operated at 200 kV for HAADF STEM imaging and energy-dispersive spectroscopy (EDS). The convergence semi-angle and beam current during imaging were 18 mrad and 60 pA, respectively, unless otherwise noted.

The RevSTEM data were processed using a custom MATLAB script to remove drift and scan distortion (Sang & LeBeau, 2014). Ten datasets for Bi_2Te_3, Bi_2Se_3 and $Bi_2Te_{2.7}Se_{0.3}$ were acquired with 20 1,024 × 1,024 pixel frames with a 3 μs dwell time. In the case of the alloy, five grains were sampled and eight series were analyzed from each grain. For calibration, ten <100> Si image series were collected immediately following acquisition of data from Bi_2Se_3, Bi_2Te_3, and $Bi_2Te_{2.7}Se_{0.3}$. For consistent RevSTEM calibration, the scan orientation was fixed throughout the study. Each Si dataset was processed to obtain both the global distortion parameters and pixel size calibration. The standard deviation and standard error were 0.07% and 0.01%, respectively. The mean for the pixel calibration and global distortion parameters were used throughout the remainder of data processing.

The STEM was also equipped with a FEI SuperX EDS detector. Spectra for composition determination were collected with a 200 pA probe for ~10 min, and contained well over a million counts. In order to minimize the effects of channelling, each map was acquired at an off-zone axis condition. The Bruker Espirit software was used for post-processing, using estimated *k*-factors for composition determination. Atomic resolution EDS maps were collected with the sample aligned along the <100> zone axis and with a probe current of 100 pA. The characteristic X-rays used for analysis were: Bi-M_{ab}, Te-K, and Se-L. A three-pixel smoothing filter was applied to the atomic resolution maps.

XRD

High-resolution XRD patterns were measured at the Argonne National Laboratory Advanced Photon Source 11-BM-B beamline. Bi_2Se_3, Bi_2Te_3, and $Bi_2Te_{2.7}Se_{0.3}$ powders were mixed with nanocrystalline SiO_2 to minimize X-ray absorption. Diffraction patterns were measured over a 2θ range of 2–50° with a 0.001° step-size using 30 keV (0.413849 Å) X-rays. Bond length and lattice parameters of Bi_2Se_3, Bi_2Te_3, and $Bi_2Te_{2.7}Se_{0.3}$ were determined by crystallographic structure refinement using the Rietveld analysis software General Structure Analysis System (GSAS) with the EXPGUI interface (Toby, 2001; Larson and Von Dreele, 2004). Parameters refined included the background, zero, profile shape, scale, lattice, atomic positions, isotropic displacement, and atomic site occupancies. The background was modeled using a 14th order Chebyshev polynomial. A high order background model was necessary to account for the amorphous scattering from nanocrystalline SiO_2.

Five XRD patterns of Bi_2Se_3, Bi_2Te_3, and $Bi_2Te_{2.7}Se_{0.3}$ were also measured using a PANalytical Empyrean to interrogate the precision and estimate the uncertainty of

lattice parameters measured by XRD. Diffraction patterns were measured over a 2θ range of 5–100° with a 0.013° step size. Lattice parameters of a and c were determined by lattice parameter refinement using Rietveld analysis software GSAS with the EXPGUI interface. Lattice parameter error was determined from the 95th confidence interval of the Rietveld refinement least-squares fit.

DFT

DFT calculations were performed with the Vienna Ab initio Simulation Package (VASP) with a plane-wave basis set, as implemented in VASP 5.3, using the recommended GW pseudopotentials supplied with VASP, which are based on the pseudopotentials of Perdew, Burke, and Ernzerhof (PBE; Kresse & Hafner, 1993, 1994; Blöchl, 1994; Perdew et al., 1996, 1997; Kresse & Furthmüller, 1996a, 1996b; Kresse & Joubert, 1999). These pseudopotentials yield similar results to the regular PBE pseudopotentials for ordinary DFT calculations, but are fit to better reproduce scattering properties at high energies, which is important for RPA calculations. Fifteen electrons were modeled explicitly per Bi atom, while six electrons were modeled explicitly for each Te and Se atom.

All DFT calculations were performed using primitive rhombohedral cells containing five atoms. The DFT relaxation used a 1,331 k-point mesh before symmetry reduction and a plane wave energy cutoff of 325 eV. The adiabatic-connection fluctuation–dissipation theorem in the random phase approximation (ACFDT-RPA) calculations were performed with a 27 k-point mesh before symmetry reduction. Long-wavelength contributions from the polarizability were neglected in the RPA calculations, which improves convergence with respect to k-points for metals, and a correction term related to partial occupancies was added to the total energy. Bader charge analysis was performed using a code developed by the Henkelman group at UT Austin (Henkelman et al., 2006; Sanville et al., 2007; Tang et al., 2009). The analysis was carried out on the results of ordinary DFT calculations using structures optimized with both DFT and ACFDT–RPA.

Results and Discussion

To address the residual scan distortion, we imaged widely available <100> Si. The four-fold symmetry along this zone axis enables the detection and quantification of residual distortion as modeled by a global affine transformation. We first determine the location of all atom columns with sub-pixel precision and index them into a matrix representation (Sang et al., 2014). From this representation, we measure the distance of each atom column to all nth nearest neighbors and calculate the corresponding standard deviation (σ_n) as reported in Figure 2. For a typical uncalibrated RevSTEM image, distances beyond the first few nearest neighbors experience increasingly significant skew, dilation, or compression that shortens or expands measurements that should otherwise be identical (Fig. 2, circles).

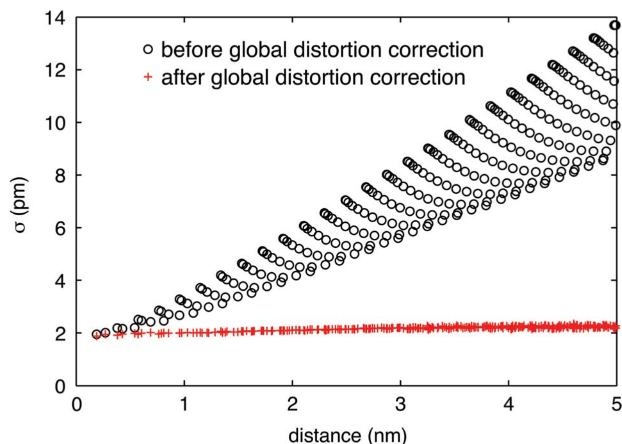

Figure 2. Standard deviation of the distance between nth near-neighbor atom columns measured for <100> Si before and after correcting residual scan distortion.

For an ideal STEM image, σ_n values should be identical for all nth neighbor pair distances, i.e. σ_n should be small and independent of nth neighbor pair distance. The linear residual distortion can be modeled as an affine transformation, T, defined as

$$T = \begin{pmatrix} 1 & 0 \\ x_1 & 1 + x_2 \end{pmatrix} \tag{1}$$

where x_1 and x_2 are the shear and expansion/contraction components, respectively. We utilize a calibration algorithm that determines the coefficients by a least squares fit minimizing the sum of σ_n^2. Once the coefficients are identified and applied to the Si dataset, σ_n is consistently 2 pm even for atom column pairs 5 nm apart as in Figure 2. To investigate calibration stability, a series of ten Si RevSTEM images were collected and analyzed in the manner outlined above. The calibration standard deviation was 0.07% for the ten images. To ensure that scan distortion remains stable over time, three sets of Si (001) data were acquired, separated by 12 h between the first and second and 1 week between the first and third set, resulting in a difference of 0.04 and 0.07%, respectively. The observed stability indicates that the measured RevSTEM calibration factors can be used with confidence across multiple days, and are not limited to a single image.

Once the scan system is accurately calibrated with the procedure outlined above, crystallographic parameters for the chalcogenide samples can be determined. Along the <100> projection of the Bi_2Te_3 structure (space group $R\overline{3}m$), two lattice parameters, a and c, are accessible. This is presented schematically in Figure 3a where only a few of the 721 unit cells in the image are highlighted. Furthermore, the standard deviation of the c lattice parameters within the image was 5.8 pm, corresponding to 0.2% variation. Using the hexagonal space group setting, the Bi_2Te_3 and Bi_2Se_3 lattice parameters from the average of ten RevSTEM images and an average of five XRD patterns measured using a laboratory diffractometer are compared with previous literature in Table 1. Notably, the RevSTEM measurements

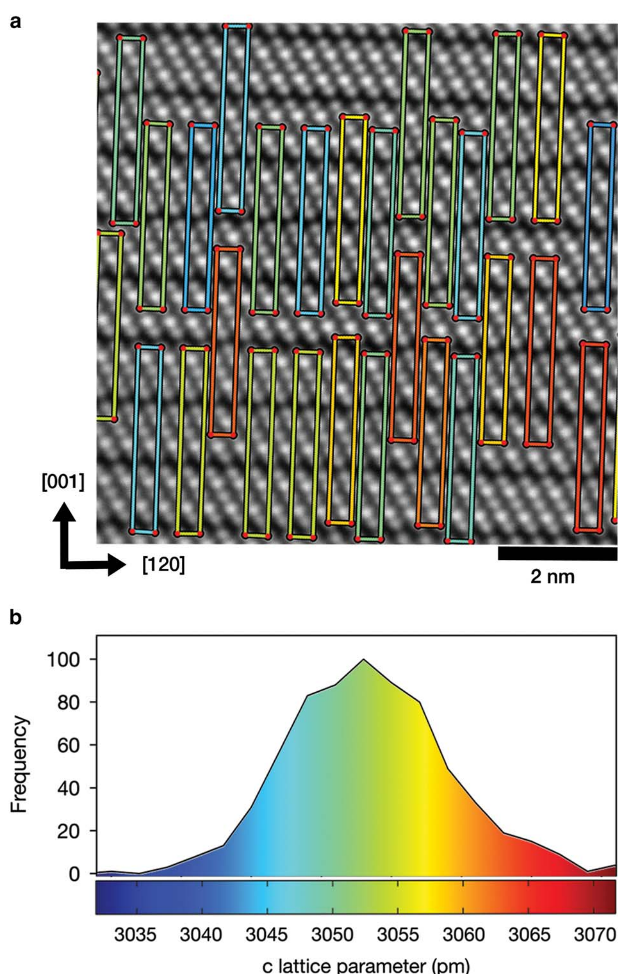

Figure 3. a: High-angle annular dark-field scanning transmission electron microscopy (HAADF STEM) image of pure Bi_2Te_3 along <100> with the rectangles representing a few of the individual projected unit cells in the image. The color of each rectangle corresponds to the color scale in (**b**). **b:** Histogram of *c* lattice parameters for one RevSTEM image.

are in excellent agreement with both our XRD measurements and prior literature, with 0.06 and 0.01% error for Bi_2Se_3 and Bi_2Te_3, respectively (Nakajima, 1963; Park et al., 2013). Moreover, the average measurement standard deviation is within a picometer for the *a* lattice parameter and under four picometers for *c*, translating to a standard error below 0.1%. While slight crystal misalignment can introduce small, relative shifts in atom positions, the repeat unit is unaffected (So & Kimoto, 2012).

With the accuracy and precision of RevSTEM validated for the pure compounds, lattice parameters of the nanostructured $Bi_2Te_{2.7}Se_{0.3}$ alloy are measured. The average lattice parameters from five different grains are also reported in Table 1. The error between the average in RevSTEM images and XRD is again below 0.1%. Moreover, because the lattice parameters of $Bi_2Te_{3-x}Se_x$ alloys obey a linear relationship for $x < 1$, they conform to Vegard's law (Wiese & Muldawer, 1960; Nakajima, 1963). This indicates that composition can be inferred with a high degree of accuracy directly from lattice parameter measurements. Using the STEM and XRD measured *c* lattice parameter, the calculated Se content of the nanostructured alloy is 6.8 ± 0.66 at% ($x \approx 0.3$) and 6.35 ± 0.03 at%, respectively, using a 95% confidence interval. Independent analysis with EDS indicated that the average Se composition is 6.54 ± 0.20 at%. This excellent agreement demonstrates the opportunity for RevSTEM to directly correlate lattice parameters with local variations in nanoscale chemical fluctuation.

Beyond unit cell measurements, real-space analysis also enables access to atom positions within the unit cell. The full definition of the Bi_2Te_3 crystal structure requires the fractional coordinates of the Bi, VI^1, and VI^2 sites within the structure. Defined by *u* and *v* in the hexagonal setting, the atomic positions are as follows: Bi (0, 0, *u*), VI^1 (0, 0, *v*), VI^2 (0, 0, 0). As demonstrated in Table 1, the *u* and *v* RevSTEM measurements are in excellent agreement with results from crystallographic structure refinements of high-resolution synchrotron XRD data and previous studies (Nakajima, 1963).

Quantitative RevSTEM measurements paired with atomic resolution spectroscopy enable direct identification of atom site preference (Allen et al., 2015). The elemental identity of each atom column is determined with atomic resolution EDS (Fig. 4a). Comparison of experimental and simulated EDS maps reveals preferential segregation of Se to Te^2 crystal positions (Fig. 4b), in agreement with prior literature (Jiang et al., 2013; Park et al., 2013). Importantly, Se is more electronegative than Te, and thus the Se-Bi bonds are expected to be more ionic than Te-Bi (Nakajima, 1963). As a result, we also expect bond length changes to occur within the layered structure.

The bond lengths and van der Waals gap can be accurately inferred utilizing the known Bi_2Te_3 crystal symmetry as shown in Figure 4b. The bond lengths are extracted from high-resolution synchrotron XRD data by crystallographic structure analysis using the Rietveld method, and calculated from STEM images using projected distances between neighboring atom columns in the quintuple, d_{proj}, and distances between like atom columns in neighboring quintuples, a_{proj}. The bond lengths are then calculated using the following equation: bond length $= \sqrt{d_{\text{proj}}^2 + 1/3a_{\text{proj}}^2}$. As with the fractional coordinates, the measured bond length values for pure compounds of Bi_2Te_3 and Bi_2Se_3 are in excellent agreement with the literature and Rietveld analysis, see Figure 4c (Nakajima, 1963; Park et al., 2013). While $Bi_2Te_{2.7}Se_{0.3}$ alloy bond lengths within the quintuple layer lie between the values of Bi_2Te_3 and Bi_2Se_3, the nearest neighbor distance across the van der Waals gap increases anomalously. Although the VI^1-Bi and VI^2-Bi bonds exhibit similar character as a function of Se content, the van der Waals gap is controlled by longer range interactions (Drabble & Goodman, 1958; Nakajima, 1963; Park et al., 2013).

To understand the origins of the increased van der Waals gap for the alloy relative to the pure phases, DFT was used to calculate the atomic structure of Bi_2Te_3, Bi_2Te_2Se, and Bi_2Se_3. Rather than directly modeling the alloy, we have instead

Table 1. Measured Bi_2Te_3, Bi_2Se_3, and $Bi_2Te_{2.7}Se_{0.3}$ Lattice Parameters, a and c, and Fractional Atom Positions, u and v, for STEM and XRD ± one Standard Error.

Lattice Parameters	Bi_2Te_3 (pm)	Bi_2Se_3 (pm)	$Bi_2Te_{2.7}Se_{0.3}$ (pm)
c			
Ref. (Nakajima, 1963)	3,049.7	2,863.6	–
XRD (S)	3,050.23 ± 0.03	2,863.94 ± 0.02	3,030.51 ± 0.02
XRD (L)	3,050.11 ± 0.02	2,864.10 ± 0.04	3,030.43 ± 0.04
STEM	3,049.28 ± 1.17	2,861.92 ± 0.93	3,028.04 ± 1.05
a			
Ref. (Nakajima, 1963)	438.6	414.3	–
XRD (S)	438.48 ± 0.003	414.01 ± 0.01	435.50 ± 0.01
XRD (L)	438.44 ± 0.004	414.00 ± 0.01	435.56 ± 0.01
STEM	438.16 ± 0.12	413.93 ± 0.07	435.14 ± 0.33
Atom Positions	**Bi_2Te_3**	**Bi_2Se_3**	**$Bi_2Te_{2.7}Se_{0.3}$**
u			
Ref. (Nakajima, 1963)	0.4000	0.4008	–
XRD(S)	0.4004 ± 0.0001	0.4009 ± 0.0001	0.3987 ± 0.0001
STEM	0.3984 ± 0.0008	0.4017 ± 0.0007	0.3990 ± 0.0010
v			
Ref. (Nakajima, 1963)	0.2095	0.2117	–
XRD(S)	0.2094 ± 0.0001	0.2108 ± 0.0001	0.2105 ± 0.0001
STEM	0.2078 ± 0.0004	0.2100 ± 0.0004	0.2117 ± 0.0005

XRD, X-ray diffraction; STEM, scanning transmission electron microscopy.
(S) and (L) correspond to data from synchrotron and laboratory XRD experiments, respectively.

considered the compound Bi_2Te_2Se such that every VI^2 site is occupied by Se. This is a good approximation as experimental observations confirm that Se tends to occupy the VI^2 layer until it is completely filled (Park et al., 2013). It is well known that, while DFT is often accurate at calculating structural parameters for strongly bonded materials, the ability to accurately model van der Waals bonding is poor. Rather, the ACFDT-RPA is a method of obtaining a very accurate electron correlation energy, which when added to the Hartree–Fock exact exchange energy yields accurate total energies for a given system (Harl & Kresse, 2008, 2009; Harl et al., 2010). It has been demonstrated that ACFDT-RPA can describe van der Waals bonding in solids more accurately than alternative theoretical methods, albeit at a much higher computational cost than traditional DFT (Björkman et al., 2012). For these reasons, we varied the relaxed structure obtained from traditional DFT in such a manner that only the VI^1-VI^1 bond length would change, and calculated the ACFDT-RPA total energy for each variation to determine the minimum-energy bond length across the van der Waals gap.

The bond lengths across the van der Waals gap, as predicted by this procedure, are presented in Table 2. Under the assumption that Vegard's law for the lattice parameters is valid for compositions within the range from Bi_2Te_3 to Bi_2Te_2Se, we used linear interpolation of the lattice parameters to estimate the bond lengths for $Bi_2Te_{2.7}Se_{0.3}$ from the DFT data. The results of this interpolation yield estimations of the strong bond lengths within 1.25% of the STEM measurements on the alloy, and an estimation of the van der Waals bond length with <3% difference from the STEM measurements. Perhaps most importantly, the anomalous increase in the size of the van der Waals gap for the alloy composition relative to both of the pure phases is reflected in the results of the ACFDT-RPA calculations.

We also performed Bader charge analysis in order to calculate the relative charge on each atom in the unit cell for each composition with the results tabulated in Table 3. While the Bader analysis was performed for structures predicted with the assistance of the ACFDT-RPA method, it is important to note that it is the result of traditional DFT calculations as the applied implementation of ACFDT-RPA does not output charge density data. The Se atoms are more negatively charged than Te atoms in equivalent positions, consistent with their relative electronegativities; correspondingly, the positive charge on the Bi atoms increases as a function of Se content in order to balance the extra negative charge.

The observed and calculated increase in the VI^1-VI^1 bond length with increasing Se content in $Bi_2Te_{2.7}Se_{0.3}$ for $x < 1$ can be attributed to the corresponding increase in the magnitudes of the charge on VI^1 and Bi. The higher positive charge on Bi attracts the slightly higher negative charge on VI^1 more strongly than for pure Bi_2Te_3, which results in a more pronounced permanent dipole on VI^1, thereby enhancing the forces from the secondary bonds. The permanent dipole moments of VI^1 atoms on either side of the van der Waals gap are oriented in opposite directions, leading to a repulsive interaction. Therefore, larger dipoles in the alloy lead to a larger van der Waals gap relative to pure

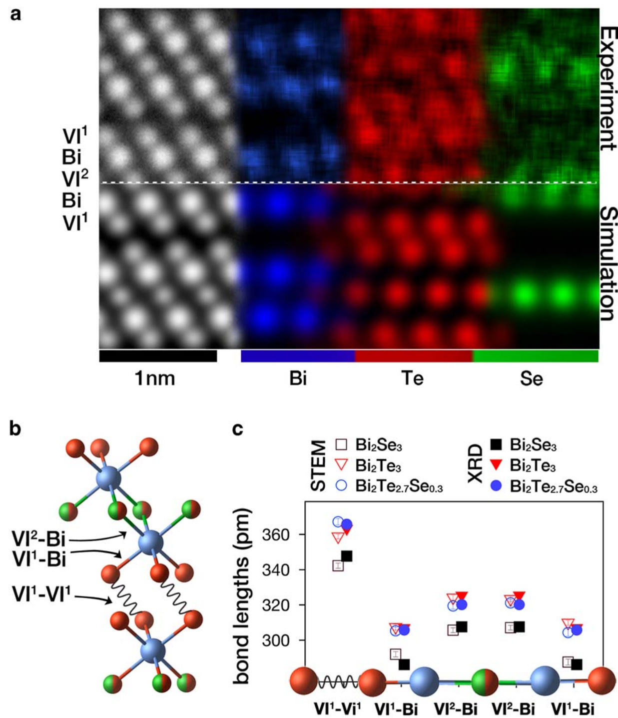

Figure 4. a: HAADF STEM and atomic resolution EDS maps of $Bi_2Te_{2.7}Se_{0.3}$ aligned along <100>. The preferential segregation of Se in the structure is clearly revealed (probe convergence semi-angle 13.5 mrad). **b:** Schematic $Bi_2Te_{2.7}Se_{0.3}$ alloy structure for each atom row and bond type. **c:** Bond lengths in the quintuple layer structure measured using RevSTEM and XRD.

Bi_2Te_3. Increased Se content to compositions of $x > 1$ leads to eventual population of VI^1 sites with Se. Although the charge separation continues to increase, the smaller radius of Se relative to Te causes the van der Waals gap to shorten once again as Se content approaches that of Bi_2Se_3.

Table 2. Measured Bi_2Te_3, Bi_2Se_3, and $Bi_2Te_{2.7}Se_{0.3}$ bond distances Using STEM and DFT. Theory values for $Bi_2Te_{2.7}Se_{0.3}$ were calculated using a linear interpolation via Vegard's Law between Bi2Te3 and Bi2Te2Se.

Bond Type	Technique	Bi_2Te_3 (pm)	Bi_2Se_3 (pm)	$Bi_2Te_{2.7}Se_{0.3}$ (pm)
VI^1-VI^1	Theory	365	328	372
	STEM	358.9 ± 1.4	342.3 ± 1.5	367.2 ± 1.9
	XRD	363.27 ± 0.08	347.70 ± 0.01	365.79 ± 0.05
Bi-VI^1	Theory	309	2.88	308
	STEM	308.7 ± 1.6	289.8 ± 1.6	304.9 ± 2.2
	XRD	306.95 ± 0.06	286.24 ± 0.01	305.78 ± 0.04
Bi-VI^2	Theory	328	310	323
	STEM	323.8 ± 1.4	306.4 ± 1.3	320.3 ± 1.8
	XRD	325.45 ± 0.05	307.59 ± 0.01	320.18 ± 0.03

STEM, scanning transmission electron microscopy; DFT, density functional theory; XRD, X-ray diffraction; ACFDT-RPA, adiabatic-connection fluctuation–dissipation theorem in the random phase approximation.
The van der Waals gap size was determined by applying ACFDT-RPA.

Table 3. Charge per ion via Bader Analysis.

Atom Type	Bi_2Te_3	Bi_2Te_2Se	Bi_2Se_3
VI^1	−0.38	−0.40	− 0.58 (Se)
Bi	0.69	0.81	1.00
VI^2	−0.61	−0.82 (Se)	− 0.83 (Se)

Conclusions

We have shown that calibrated RevSTEM imaging achieves highly accurate structural quantification at the nanoscale. These lab-scale capabilities advance real-space structure determination that complement well-established synchrotron powder diffraction methods. Localized information regarding structure and chemistry can be obtained to compare against the average structure determined from diffraction data, thus providing a more complete characterization of nanostructured materials. We have also demonstrated that the combination of traditional DFT with the ACFDT-RPA method provides structural parameters of Bi_2Te_3, Bi_2Te_2Se, Bi_2Se_3, and (via Vegard's Law) $Bi_2Te_{2.7}Se_{0.3}$, in good agreement with experiment. Further, through the use of Bader charge analysis, we have shown that the anomalous increase in the size of the van der Waals gap for $Bi_2Te_{2.7}Se_{0.3}$ can be attributed to a corresponding increase in the repulsion between permanent dipoles on either side of the gap. Overall, these results demonstrate that atomic resolution imaging using electrons can provide accurate and precise direct quantitative crystallographic analysis to relate composition, bonding, and structure at the nanoscale.

Acknowledgements

J.H.D., X.S., and J.M.L. gratefully acknowledge support from the Air Force Office of Scientific Research (Grant No. FA9550-14-1-0182). J.H.D. acknowledges support for this work by the National Science Foundation Graduate Research Fellowship (Grant DGE-1252376). J.S.H. and D.L.I. acknowledge support for the DFT work from a grant from the National Science Foundation, DMR-1151568. T.E.C. and C.C.K. acknowledge support through DARPA/DSO (Contract W911NF-08-C--0058). The authors acknowledge the use of the Analytical Instrumentation Facility (AIF) at North Carolina State University, which is supported by the State of North Carolina and the National Science Foundation. S.D.F. and L.J.A. were supported under the Discovery Projects funding scheme of the Australian Research Council (Projects DP140102538 and DP110102228). Use of the Advanced Photon Source at Argonne National Laboratory was supported by the U.S. Department of Energy, Office of Science, Office of Basic Energy Sciences (Contract DE-AC02-06CH11357).

References

Allen, L., D'Alfonso, A. & Findlay, S. (2015). Modelling the inelastic scattering of fast electrons. *Ultramicroscopy* **151**, 11–22.

Billinge, S.J.L. & Levin, I. (2007). The problem with determining atomic structure at the nanoscale. *Science* **316**, 561–565.

Björkman, T., Gulans, A., Krasheninnikov, A.V. & Nieminen, R.M. (2012). Are we van der Waals ready? *J Phys Condens Matter* **24**, 424218.

Blöchl, P.E. (1994). Projector augmented-wave method. *Phys Rev B* **50**, 17953.

Chan, T.-T.E., LeBeau, J.M., Venkatasubramanian, R., Thomas, P., Stuart, J. & Koch, C.C. (2013). Carrier concentration modulation by hot pressing pressure in n-type nanostructured Bi(Se)Te alloy. *Appl Phys Lett* **103**, 144106.

Denton, A.R. & Ashcroft, N.W. (1991). Vegard's law. *Phys Rev A* **43**, 3161–3164.

Drabble, J.R. & Goodman, C.H.L. (1958). Chemical bonding in bismuth telluride. *J Phys Chem Solids* **5**, 142–144.

Dycus, J.H., White, R.M., Pierce, J.M., Venkatasubramanian, R. & LeBeau, J.M. (2013). Atomic scale structure and chemistry of Bi2Te3/GaAs interfaces grown by metallorganic van der Waals epitaxy. *Appl Phys Lett* **102**, 081601–081601-4.

Esteves, G., Fancher, C.M. & Jones, J.L. (2014). In situ characterization of polycrystalline ferroelectrics using x-ray and neutron diffraction. *J Mater Res* **30**, 340–356.

Harl, J. & Kresse, G. (2008). Cohesive energy curves for noble gas solids calculated by adiabatic connection fluctuation-dissipation theory. *Phys Rev B* **77**, 045136.

Harl, J. & Kresse, G. (2009). Accurate bulk properties from approximate many-body techniques. *Phys Rev Lett* **103**, 056401.

Harl, J., Schimka, L. & Kresse, G. (2010). Assessing the quality of the random phase approximation for lattice constants and atomization energies of solids. *Phys Rev B* **81**, 115126.

Henkelman, G., Arnaldsson, A. & Jónsson, H. (2006). A fast and robust algorithm for bader decomposition of charge density. *Comput Mater Sci* **36**, 354–360.

Jiang, Y., Wang, Y., Sagendorf, J., West, D., Kou, X., Wei, X., He, L., Wang, K.L., Zhang, S. & Zhang, Z. (2013). Direct atom-by-atom chemical identification of nanostructures and defects of topological insulators. *Nano Lett* **13**, 2851–2856.

Kim, Y.-M., He, J., Biegalski, M.D., Ambaye, H., Lauter, V., Christen, H.M., Pantelides, S.T., Pennycook, S.J., Kalinin, S.V. & Borisevich, A.Y. (2012). Probing oxygen vacancy concentration and homogeneity in solid-oxide fuel-cell cathode materials on the subunit-cell level. *Nat Mater* **11**, 888–894.

Kimoto, K., Asaka, T., Yu, X., Nagai, T., Matsui, Y. & Ishizuka, K. (2010). Local crystal structure analysis with several picometer precision using scanning transmission electron microscopy. *Ultramicroscopy* **110**, 778–782.

Kresse, G. & Furthmüller, J. (1996a). Efficiency of ab-initio total energy calculations for metals and semiconductors using a plane-wave basis set. *Comput Mater Sci* **6**, 15–50.

Kresse, G. & Furthmüller, J. (1996b). Efficient iterative schemes for ab initio total-energy calculations using a plane-wave basis set. *Phys Rev B* **54**, 11169.

Kresse, G. & Hafner, J. (1993). *Ab initio* molecular dynamics for liquid metals. *Phys Rev B* **47**, 558–561.

Kresse, G. & Hafner, J. (1994). Ab initio molecular-dynamics simulation of the liquid-metal-amorphous-semiconductor transition in germanium. *Phys Rev B* **49**, 14251.

Kresse, G. & Joubert, D. (1999). From ultrasoft pseudopotentials to the projector augmented-wave method. *Phys Rev B* **59**, 1758.

Lan, Y., Poudel, B., Ma, Y., Wang, D., Dresselhaus, M.S., Chen, G. & Ren, Z. (2009). Structure study of bulk nanograined thermoelectric bismuth antimony telluride. *Nano Lett* **9**, 1419–1422.

Larson, A.C. & Von Dreele, R.B. (2004). General Structure Analysis System (GSAS). Los Alamos National Laboratory Report No. Laur 86-748 (unpublished).

Martin, J., Wang, L., Chen, L. & Nolas, G.S. (2009). Enhanced Seebeck coefficient through energy-barrier scattering in PbTe nanocomposites. *Phys Rev B* **79**, 115311.

Nakajima, S. (1963). The crystal structure of $Bi_2Te_{3-x}Se_x$. *J Phys Chem Solids* **24**, 479–485.

Page, K., Proffen, T., Niederberger, M. & Seshadri, R. (2010). Probing local dipoles and ligand structure in BaTiO 3 nanoparticles. *Chem Mater* **22**, 4386–4391.

Park, K., Nomura, Y., Arita, R., Llobet, A. & Louca, D. (2013). Local strain and anharmonicity in the bonding of $Bi_2Se_{3Gx}Te_x$ topological insulators. *Phys Rev B* **88**, 224108.

Pennycook, S.J. & Nellist, P.D. (2011). *Scanning transmission electron microscopy: Imaging and analysis*. Springer-Verlag, New York.

Perdew, J.P., Burke, K. & Ernzerhof, M. (1996). Generalized gradient approximation made simple. *Phys Rev Lett* **77**, 3865.

Perdew, J., Burke, K. & Ernzerhof, M. (1997). Generalized gradient approximation made simple [Phys Rev Lett 77, 3865 (1996)] *Phys Rev Lett* **78**, 1396–1396.

Poudel, B., Hao, Q., Ma, Y., Lan, Y., Minnich, A., Yu, B., Yan, X., Wang, D., Muto, A., Vashaee, D., Chen, X., Liu, J., Dresselhaus, M.S., Chen, G. & Ren, Z. (2008). High-thermoelectric performance of nanostructured bismuth antimony telluride bulk alloys. *Science* **320**, 634–638.

Sang, X. & LeBeau, J.M. (2014). Revolving scanning transmission electron microscopy: Correcting sample drift distortion without prior knowledge. *Ultramicroscopy* **138**, 28–35.

Sang, X., Oni, A.A. & LeBeau, J.M. (2014). Atom column indexing: Atomic resolution image analysis through a matrix representation. *Microsc Microanal* **20**, 1764–1771.

Sanville, E., Kenny, S.D., Smith, R. & Henkelman, G. (2007). Improved grid-based algorithm for bader charge allocation. *J Comput Chem* **28**, 899–908.

So, Y.-G. & Kimoto, K. (2012). Effect of specimen misalignment on local structure analysis using annular dark-field imaging. *J Electron Microsc (Tokyo)* **61**, 207–215.

Tang, W., Sanville, E. & Henkelman, G. (2009). A grid-based bader analysis algorithm without lattice bias. *J Phys Condens Matt* **21**, 084204.

Thomas, J.M. (2012). Centenary: The birth of X-ray crystallography. *Nature* **491**, 186–187.

Toby, B.H. (2001). Expgui, a graphical user interface for GSAS. *J Appl Crystallogr* **34**, 210–213.

Wiese, J.R. & Muldawer, L. (1960). Lattice constants of Bi2Te3-Bi2Se3 solid solution alloys. *J Phys Chem Solids* **15**, 13–16.

Yankovich, A.B., Berkels, B., Dahmen, W., Binev, P., Sanchez, S.I., Bradley, S.A., Li, A., Szlufarska, I. & Voyles, P.M. (2014). Picometre-precision analysis of scanning transmission electron microscopy images of platinum nanocatalysts. *Nat Commun* **5**, 4155.